# Direct Numerical Simulation of Discrete Roughness on a Swept-Wing Leading Edge

Donald P. Rizzetta[*] and Miguel R. Visbal[†]

*U.S. Air Force Research Laboratory, Wright-Patterson Air Force Base, Ohio 45433-7512*

and

Helen L. Reed[‡] and William S. Saric[§]

*Texas A&M University, College Station, Texas 77843-3141*

Direct numerical simulation is employed in order to describe the subsonic flow past an array of micron-sized discrete roughness elements, which were mounted near the leading edge of a 30-degree swept wing at a chord Reynolds number of $7.4 \times 10^6$. The flow conditions correspond to flight receptivity experiments that were conducted to investigate the effects of roughness on crossflow instabilities. To make the computations tractable, the geometry is scaled by the radius of the wing leading edge, which magnifies the region of interest and enhances resolution. The leading-edge region is then approximated by the flow past an infinite parabolic cylinder. The numerical method is based upon a sixth-order-accurate time-implicit scheme to attain high fidelity and was used in conjunction with an eighth-order low-pass Padé-type nondispersive filter operator to maintain stability. A high-order overset-grid approach preserved spatial accuracy on a local mesh system representing the roughness elements, using domain decomposition to perform calculations on a parallel computing platform. The direct simulation for the flow about the roughness elements was used to capture crossflow vortices and served as input to the nonlinear parabolized stability equations, which were then solved in order to determine receptivity of the flow to the geometric perturbations. Three different geometric roughness elemental shapes were investigated in the study. For one shape, the effect of element height was examined. Features of the roughness-element flowfields are elucidated, and findings of the stability calculations are compared. Results are presented for receptivity of the crossflow instability to the size and shape of elements, as obtained by the direct numerical simulation and by two different stability approaches.

## Nomenclature

| | | |
|---|---|---|
| $\mathcal{A}_{n,k}$ | = | wave function amplitude for nonlinear parabolized stability equations |
| $A_{u'_t}$ | = | amplitude of the maximum tangential velocity perturbation |
| $\mathcal{B}_i, \mathcal{C}_i, \mathcal{D}_i$ | = | coefficient matrices for nonlinear parabolized stability equations |
| $C_p$ | = | pressure coefficient |
| $d$ | = | dimensional roughness-element diameter, 0.002 m |
| $E$ | = | total specific energy |
| $\boldsymbol{F}, \boldsymbol{G}, \boldsymbol{H}$ | = | inviscid vector fluxes |
| $F_{u'_t}$ | = | spatial spanwise frequency spectra of the maximum tangential velocity perturbation |
| $\boldsymbol{F}_v, \boldsymbol{G}_v, \boldsymbol{H}_v$ | = | viscous vector fluxes |
| $h$ | = | dimensional roughness-element height |
| $I, J, K$ | = | grid indices in body circumferential, body normal, and spanwise directions |
| $\mathcal{J}$ | = | Jacobian of the coordinate transformation |
| $k$ | = | planar integrated perturbation kinetic energy |
| $k_s$ | = | scaled planar integrated perturbation kinetic energy |
| $M$ | = | Mach number |
| $N$ | = | natural log of stability amplitude ratio |
| $\mathcal{N}$ | = | right-hand-side vector for nonlinear parabolized stability equations |
| $n$ | = | nondimensional normal distance from parabolic surface |
| $Pr$ | = | Prandtl number, 0.73 for air |
| $p$ | = | nondimensional static pressure |
| $\boldsymbol{Q}$ | = | vector of dependent variables for direct numerical simulation |
| $\mathcal{Q}_i$ | = | components of the heat flux vector |
| $q$ | = | velocity magnitude |
| $Re$ | = | reference Reynolds number for direct numerical simulation, $\rho_\infty q_\infty r / \mu_\infty$ |
| $R_0$ | = | reference Reynolds number for nonlinear parabolized stability equations, $\rho_\infty q_\infty \delta_0 / \mu_\infty$ |
| $r$ | = | dimensional wing leading-edge radius, 0.01905 m |
| $T$ | = | nondimensional static temperature |
| $t$ | = | nondimensional time for direct numerical simulation |
| $U, V, W$ | = | contravariant velocity components |
| $u, v, w$ | = | nondimensional Cartesian velocity components in the $x$, $y$, and $z$ directions |
| $u'_t$ | = | tangential velocity perturbation, normal to the leading edge |
| $u_1, u_2, u_3$ | = | $u, v, w$ |
| $x, y, z$ | = | nondimensional Cartesian coordinates in the wing leading-edge normal, vertical, and spanwise directions |
| $x_c$ | = | streamwise direction nondimensionalized by the airfoil section chord |
| $x_1, x_2, x_3$ | = | $x$, $y$, and $z$ |
| $\alpha$ | = | angle of attack |
| $\alpha_{n,k}$ | = | modal disturbance streamwise wave number |

*Senior Research Aerospace Engineer, Computational Sciences Branch, AFRL/RBAC. Associate Fellow AIAA.

†Technical Area Leader, Computational Sciences Branch, AFRL/RBAC. Associate Fellow AIAA.

‡Professor, Department of Aerospace Engineering, MS 3141. Fellow AIAA.

§Distinguished Professor, Department of Aerospace Engineering, MS 3141. Fellow AIAA.

| $\beta_0$ | = | fundamental disturbance spanwise wave number |
| $\gamma$ | = | specific heat ratio, 1.4 for air |
| $\Delta Q$ | = | $Q^{p+1} - Q^p$ |
| $\Delta t$ | = | time-step size |
| $\delta$ | = | nondimensional boundary-layer thickness |
| $\delta_{ij}$ | = | Kronecker delta function |
| $\delta_0$ | = | boundary-layer reference length |
| $\delta_{\xi 2}, \delta_{\eta 2}, \delta_{\zeta 2},$ $\delta_{\xi 6}, \delta_{\eta 6}, \delta_{\zeta 6}$ | = | second-order and sixth-order finite difference operators in $\xi$, $\eta$, and $\zeta$ |
| $\Lambda$ | = | wing leading-edge sweep angle, 30 deg |
| $\lambda$ | = | spanwise roughness-element spacing, 0.0045 m |
| $\mu$ | = | nondimensional molecular viscosity coefficient |
| $\xi, \eta, \zeta$ | = | nondimensional body-fitted computational coordinates for direct numerical simulation |
| $\xi_g, \eta_g$ | = | conformal orthogonal parabolic coordinates |
| $\xi_s, \eta_s, \zeta_s$ | = | nondimensional body-intrinsic computational coordinates for nonlinear parabolized stability equations |
| $\xi_t, \xi_x, \xi_y, \xi_z,$ $\eta_t, \eta_x, \eta_y, \eta_z,$ $\zeta_t, \zeta_x, \zeta_y, \zeta_z$ | = | metric coefficients of the coordinate transformation for DNS |
| $\rho$ | = | nondimensional fluid density |
| $\tau$ | = | nondimensional time for nonlinear parabolized stability equations |
| $\tau_{ij}$ | = | components of the viscous stress tensor |
| $\Phi$ | = | basic state vector of dependent variables for nonlinear parabolized stability equations |
| $\phi$ | = | vector of dependent variables for nonlinear parabolized stability equations |
| $\omega_0$ | = | fundamental disturbance temporal frequency |

*Subscripts*

| $e$ | = | evaluated at boundary-layer edge |
| $\infty$ | = | dimensional reference value |

*Superscripts*

| $n$ | = | time level |
| $p$ | = | subiteration level |
| $'$ | = | disturbance quantity |

## I.  Introduction

IT IS well known that one of the principal considerations in the design and construction of air vehicles is that of configuration drag. This is especially true for unmanned vehicles and sensorcraft, which are primarily used for intelligence, surveillance, and reconnaissance missions requiring extensive loiter times at altitude. For this situation, a decrease in drag can increase both range and endurance and can reduce the required thrust, resulting in improved fuel economy and diminished engine noise. One method of achieving reduced drag is by maintaining laminar flow on the wings and other surfaces of the flight vehicle. Because of this, aerodynamicists and designers of aircraft have pursued the objective of sustaining laminar flow for many decades.

The route to transition on a swept wing, which precludes existence of a laminar boundary layer, is a complex process characterized by nonlinear interactions and instabilities that arise from a number of sources. Among these are attachment-line contamination, Tollmien–Schlichting waves, centrifugal instabilities, and crossflow vortices. Swept-wing transition mechanisms have been studied extensively, and a number of reviews are available that describe their basic features. These include the works of Arnal [1], Reibert and Saric [2], White et al. [3], Saric and Reed [4], Saric et al. [5], and Reed and Saric [6]. In addition, summaries of relevant experimental investigations are provided by Bippes [7] and by Kachanov [8].

Near the attachment line, the inherent instability of the boundary layer may be exacerbated by contamination from freestream disturbances. The chordwise flow is capable of generating Tollmien–Schlichting waves, but these are typically stabilized by the favorable pressure gradient produced by flow over the leading edge. Any concavity in the wing geometry or virtual surface displacement due to viscous effects may result in centrifugal instabilities and the development of Görtler vortices. Because of the coupled effect of wing sweep and pressure gradient, an inviscid instability mechanism can give rise to the formation of crossflow vortices.

The focus of the present investigation is on the stationary swept-wing crossflow instability, characteristic of flight, and its receptivity to micron-sized spanwise-periodic discrete roughness located near the leading edge. The crossflow region may contain both stationary disturbances and traveling waves [5]. Linear stability theory predicts that the unsteady disturbances have higher growth rates than the stationary ones, but both have been observed to cause transition in many experimental studies [2,5,9]. Whether stationary or traveling waves dominate is related to the receptivity process. Stationary waves are more important in the low-turbulence environments characteristic of flight, while traveling waves are more influential in high-turbulence surroundings [7,10]. In a flight environment, the presence of micron-sized three-dimensional roughness at a wing leading edge can establish a stationary streamwise vortex. A three-dimensional boundary layer is extremely sensitive to such roughness; however, the roughness has no effect on streamwise disturbances [11]. Freestream turbulence appears to be the source of the traveling crossflow instability when interacting with surface roughness, but such turbulence is not a major feature of most flight conditions [12]. Thus, in this situation, surface roughness is the most significant receptivity mechanism, and the instability evolves as a pair of stationary corotating vortices, whose axes are closely aligned with local inviscid streamlines.

To quantify the effects of roughness, Saric et al. [13] systematically applied micron-sized roughness near the leading edge of a swept wing at a chord Reynolds number of $2.4 \times 10^6$. They noted that spanwise-periodic discrete roughness elements had no effect if not applied within the first 2–5% of the chord. It was also shown that the linearly predicted most unstable mode (termed the critical mode) could be suppressed, thereby delaying transition. This was accomplished by designing the airfoil section to produce a judiciously chosen pressure distribution and by distributing roughness elements at a spacing approximately equal to one-half of the spanwise wavelength of the critical mode. When the micron-sized elements are applied at subcritical spacings, they produce a rapid growth of the forced stability mode and then decay. This forced mode then completely suppresses the critical mode, thus delaying transition beyond the natural location that would occur in the absence of any artificial roughness. Spanwise-periodic discrete roughness can therefore be used as a flow control mechanism to reduce drag and enhance performance of swept-wing air vehicles. This promising laminar flow control technique has also been demonstrated for supersonic flight [14].

Following the work of Saric et al. [13], Carpenter et al. [15,16] conducted swept-wing flight tests at chord Reynolds numbers of $6.5 \times 10^6$ to $7.5 \times 10^6$, which are typical of transport aircraft. When distributed roughness elements were subcritically spaced, they were found to be effective in delaying transition. An important objective of the flight experiments was to understand the receptivity mechanism for crossflow instabilities due to the introduction of various configurations of artificial roughness near the wing leading edge and to provide validation data for companion computations. It was observed that there was high sensitivity to both the shape and height of the roughness elements.

Most of the theoretical and computational analyses, which have supplemented experiments of swept boundary layers, considered only flat surfaces with adverse pressure gradients. Thus, curvature and other nonparallel effects were not taken into account. Receptivity to surface perturbations was considered by Crouch [17] and by Choudhari [18], who prescribed the undisturbed mean flow by the Falkner–Skan–Cooke solution to the boundary-layer equations for

the flow over a uniform swept wedge. The stability computations of Ng and Crouch [19] were based upon the locally parallel flow approximation and also neglected surface curvature. Despite these simplifications, their results for roughness-induced crossflow vortices on a swept wing compared well with experimental data. Bertolotti [20] carried out similar receptivity calculations using both a Fourier-transform technique and the linearized Navier–Stokes equations. His results confirmed that receptivity characteristics may be considerably altered when nonparallel effects are taken into account. The linearized Navier–Stokes equations were also considered by Collis and Lele [21] for surface roughness near the leading edge of a swept wing. They concluded that receptivity is modified by both curvature and nonparallel influences, which are competing processes. This conclusion was also reached by Janke [22], who solved the linearized Navier–Stokes equations as well. Joslin and Streett [23] neglected curvature terms and employed a surface suction and blowing boundary condition to generate crossflow vortices that were captured by the linearized Navier–Stokes equations.

More recent computational efforts have been able employ a higher degree of sophistication, eliminating the need for previous simplifying assumptions. The work of Haynes and Reed [24] clearly demonstrated both the efficiency and accuracy of the nonlinear parabolized stability equations, which were used to simulate swept-wing vortices. Their results again verified deficiencies of less accurate stability analyses and validated earlier experiments. Various approaches employed for investigating basic mechanisms of secondary instabilities, including experiments, nonlinear parabolized stability equations (NPSE), and direct numerical simulation (DNS), have achieved considerable success in identifying unstable frequencies, mode shapes, and growth rates [25–29]. Jiang et al. [30,31] performed direct numerical simulations of crossflow disturbances in boundary layers, but only for supersonic flows. Most closely related to the present investigation are the direct numerical simulations of Piot et al. [32,33], which considered the flow around a discrete microroughness array in the laminar boundary layer on a swept cylinder. Both stationary and traveling waves were found to appear downstream of the roughness elements, and the unsteady disturbances agreed well with linear stability theory.

The aforementioned research activities have greatly contributed to an increased understanding of the crossflow instability and the effects of discrete roughness elements on swept wings. Disturbances produced by such roughness are highly sensitive to a number of parameters, which include the height of the elements, the location of the array relative to the attachment line, the spacing between elements, and freestream conditions. Previous research efforts have shown that computational approaches such as NPSE and DNS accurately model the nonlinearities, high-frequency secondary instabilities, and breakdown process due to the crossflow instability if the proper conditions are supplied. These approaches will become more practical when models connecting physical roughness characteristics with initial and boundary conditions are validated and provided to computational codes.

The computations carried out here begin to provide accurate models for roughness. The flow conditions correspond directly to the flight receptivity experiments of Carpenter et al. [15,16] for a 30 deg swept wing with critically spaced discrete roughness elements attached near the leading edge. Roughness elements on the order of 20 $\mu$m in height are applied at 1% chord to an otherwise highly polished surface. Experiments show that the roughness-induced wavelengths dominate the disturbance growth. Local flow about the elements is represented by direct numerical simulation using a high-order computational method. The chord Reynolds number of the flight conditions is $7.4 \times 10^6$, which is representative of that for sensorcraft applications. Since it is not feasible to carry out a complete computation about the entire wing, DNS is employed only for the near region surrounding the leading edge and roughness array. Results of that simulation are then employed as upstream conditions for the NPSE. The NPSE are used to ascertain response of the flow to the roughness and evolution of the crossflow instability downstream. This work complements the previous DNS of Piot et al. [32,33] for a

more realistic specification of geometry and flow conditions and provides a higher degree of numerical fidelity than alternative receptivity approaches. Features of the flowfield are elucidated, including structure of the crossflow vortices. The effect of size and shape of the roughness elements to receptivity of the crossflow instability is explored, and results of different stability approaches are presented.

## II.   Computational Approach for the DNS

The simulations described here correspond to experiments conducted at the Texas A&M University Flight Research Laboratory [15,16], which were carried out to study effects of micron-sized spanwise-periodic discrete roughness elements mounted near the leading edge of a swept wing. The Swept-Wing In-Flight Testing (SWIFT) experimental model employed in these experiments had a leading-edge sweep angle of $\Lambda = 30$ deg and was operated at a chord-based Reynolds number of $7.4 \times 10^6$, a Mach number of 0.264, and a $-4.69$ deg angle of attack during flight conditions. The SWIFT model had a polished leading edge that, along with its specifically devised support structure and low-turbulence flight environment, precluded attachment-line contamination. No concave curvature was present in the surface geometry near the leading edge, preventing the appearance of centrifugal instabilities and Görtler vortices. The wing section geometry of the model was designed to achieve a pressure distribution that was tailored to stabilize Tollmien–Schlichting waves. These features of the SWIFT model made it possible to isolate the primary mechanism for transition to that of crossflow instabilities.

To initiate and study critical (most unstable) stationary crossflow disturbances, linear stability theory suggests that the discrete roughness elements be spaced periodically in the spanwise direction at 0.0045 m parallel to the leading edge. A schematic representation of the swept-wing model appears in Fig. 1. The wing leading edge had a radius $r = 0.01905$ m, and the discrete array of roughness elements was situated at a streamwise distance from the leading edge equal to 1.0% of the axial chord length. Roughness elements had a diameter $d = 0.002$ m and a nominal height $h = 20$ $\mu$m, but this value could be varied as part of the investigation. The interelement spanwise spacing $\lambda = 0.0045$ m was equal to the critical value.

For the DNS calculations, the geometry and computational mesh coordinates are scaled by the leading-edge radius $r$. This magnifies the area of interest and enables enhanced resolution. The wing leading edge may be approximated by a parabola and in the scaled coordinates, the computation then corresponds to the canonical problem for the flow past a swept parabolic cylinder. This approach is identical to that of Collis and Lele [21] and makes the solution accessible to direct numerical simulation. In the scaled coordinate system, the reference Reynolds number $Re$ is equal to 103,254. The correspondence between the parabolic leading edge and the SWIFT airfoil section geometry is represented in Fig. 2.

Because the parabolic cylinder does not correspond to an isolated body surrounded by a freestream, only a zero angle of attack may be represented. Thus, in order to conserve computational resources, the flow along the upper surface is considered and a symmetry condition is imposed along the $x$ axis. The computational mesh system is illustrated in Fig. 3. Figure 3a shows the far-field boundaries, and
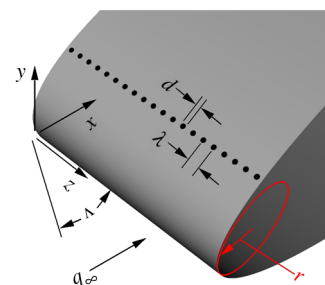


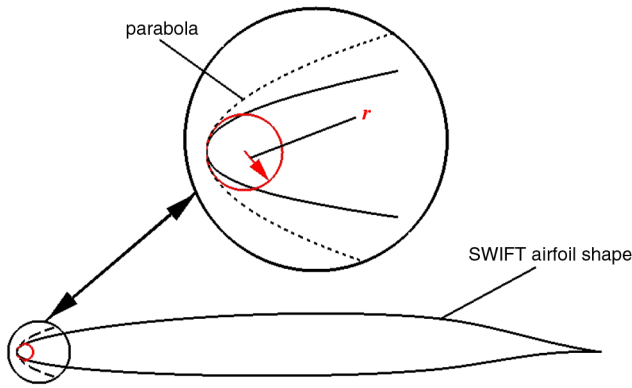**Fig. 1   Schematic representation of the swept-wing configuration.**

**Fig. 2 SWIFT airfoil section and parabolic leading-edge geometries.**

Fig. 3b indicates the grid structure near the leading edge. In this configuration, the leading edge is aligned with the spanwise $z$ axis, so that an unswept geometry is simulated, somewhat simplifying construction of the grid system. Computations by Piot et al. [32,33] and by Collis and Lele [21] also used this formulation, which then requires the freestream nondimensional velocity components to be specified as

$$u_\infty = \cos \Lambda \qquad w_\infty = \sin \Lambda \qquad (1)$$

The grid system observed in Fig. 3 was obtained by a conformal mapping of orthogonal parabolic coordinates $\xi_g$ and $\eta_g$ to the Cartesian system $x$ and $y$ according to the expression

$$x = \xi_g^2 + \frac{1 - \eta_g}{2}, \qquad y = \sqrt{2}\xi_g \eta_g \qquad (2)$$

which provides a body-fitted mesh to the surface geometry, as was also used by Collis and Lele [21]. Distributions for $\xi_g$ and $\eta_g$ were generated by automated software [34] in order to provide mesh point clustering at the parabolic surface and in the region surrounding the roughness element. A constant spacing of grid planes was used in the spanwise direction. There were $1061 \times 301 \times 121$ mesh points in the

$I$, $J$, and $K$ directions, respectively, where the $I$ direction is circumferential about the parabolic surface, the $J$ direction is orthogonal to $I$ grid lines and the body, and the $K$ direction is spanwise ($z$ direction). Only a fraction of the grid lines are shown in Fig. 3, which are clustered near the leading edge and at the roughness location in the $I$ direction and close to the body surface in the $J$ direction.

Because of the uniform arrangement of the discrete roughness, the flow is computed about a single element, and periodic conditions are specified at the spanwise boundaries, as has been done for other simulations of roughness elements [32,33,35]. Although the single-block grid topology displayed in Fig. 3 could be used for the baseline flow without roughness, an overset system is employed to represent the distributed array. This was obtained by removing a portion of the baseline mesh near the roughness location and replacing that region with a locally overset grid describing any specific roughness element. Three different geometrically shaped roughness elements were considered in this investigation: 1) cylindrical elements, 2) elements with a square base, and 3) smoothly curved elements. The length of one side of the base for the square elements is the same as the diameter of the cylindrical elements ($d$). The smoothly curved element will be referred to as a bump and has a circular base with a diameter of $d$. The height of the bump element varies parabolically as a function of radius. Simulations for all elements were carried out for a height of 20 $\mu$m. To investigate the effect of height, computations for cylindrical elements were also performed for $h = 10$ and 30 $\mu$m.

Found in Fig. 4 are the grid structures for all three roughness elements. In the cylindrical case, the element is represented by an O-grid construct to generate planes that are distributed vertically along the height of the element. Above the top of the element, the O-grid structure maintained a nonzero radius. This prevented the appearance of pole along the axis of the cylindrical grid, but resulted in the existence of a circular hole above the element. An auxiliary Cartesian mesh system was then used to fill the hole and to connect the portion of the grid above the element with the baseline mesh. For all cases, a sixth-order-accurate Lagrangian interpolation procedure [36,37] preserved spatial fidelity of the solution in the overset system. A similar methodology was successful in the simulation of Rizzetta and Visbal [35], which also considered cylindrical roughness elements.
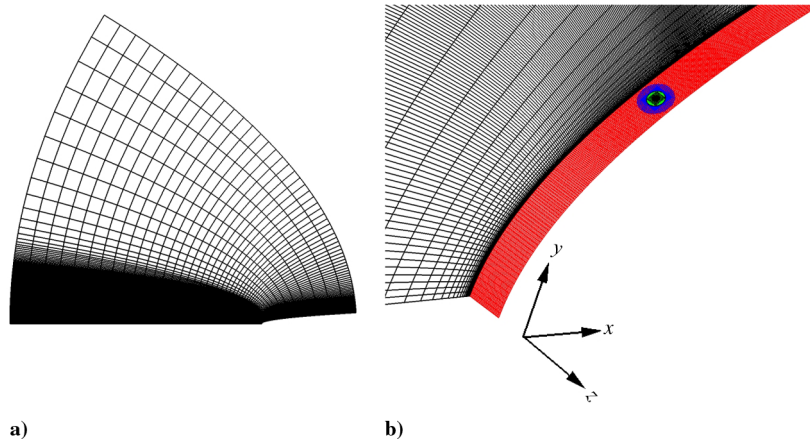


a)                                    b)

**Fig. 3 Parabolic grid structure for the swept-wing configuration: a) far-field domain and b) wing leading edge.**



cylindrical element            square element              bump element

a)                        b)                        c)

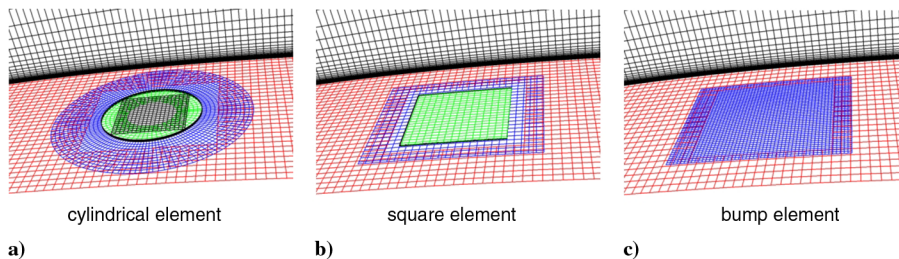**Fig. 4 Grid structure about the roughness elements for $h = 20$ $\mu$m: a) cylindrical element, b) square element, and c) bump element.**

The cylindrical grid structure depicted in Fig. 4a consists of approximately 50 points circumferentially and spanwise surrounding the element in the baseline mesh. The local grid is finer, consisting of 500 points that circle the element. In the direction normal to the top of the element, a uniform spacing is specified. The height of the element is defined by 60 points, and the uniformly spaced region extends a distance of $2h$ normal to the parabolic surface. Grid resolution for the square and bump elements is similar to that of the cylindrical mesh. Because the ratio of elemental height to diameter is small ($h/d = 0.01$), the roughness elements appear waferlike in Fig. 4.

## III. Governing Equations for the DNS

The governing fluid equations for the direct numerical simulations are taken as the unsteady three-dimensional compressible Navier–Stokes equations. After introducing a curvilinear coordinate transformation to a body-fitted system, the equations are cast in the following nondimensional conservative form:

$$\frac{\partial}{\partial t}\left(\frac{1}{\mathcal{J}}\boldsymbol{Q}\right) + \frac{\partial}{\partial \xi}\left(\boldsymbol{F} - \frac{1}{Re}\boldsymbol{F}_v\right) + \frac{\partial}{\partial \eta}\left(\boldsymbol{G} - \frac{1}{Re}\boldsymbol{G}_v\right)$$
$$+ \frac{\partial}{\partial \zeta}\left(\boldsymbol{H} - \frac{1}{Re}\boldsymbol{H}_v\right) = 0 \qquad (3)$$

Here, $t$ is the time; $\xi$, $\eta$, and $\zeta$ are the computational coordinates; $\boldsymbol{Q}$ is the vector of dependent variables; $\boldsymbol{F}$, $\boldsymbol{G}$, and $\boldsymbol{H}$ are the inviscid flux vectors, and $\boldsymbol{F}_v$, $\boldsymbol{G}_v$, and $\boldsymbol{H}_v$ are the viscous flux vectors. The vector of dependent variables is given as

$$\boldsymbol{Q} = [\rho \quad \rho u \quad \rho v \quad \rho w \quad \rho E]^T \qquad (4)$$

and the vector fluxes are given by

$$\boldsymbol{F} = \frac{1}{\mathcal{J}}\begin{bmatrix} \rho U \\ \rho u U + \xi_x p \\ \rho v U + \xi_y p \\ \rho w U + \xi_z p \\ \rho E U + \xi_{x_i} u_i p \end{bmatrix}, \qquad \boldsymbol{G} = \frac{1}{\mathcal{J}}\begin{bmatrix} \rho V \\ \rho u V + \eta_x p \\ \rho v V + \eta_y p \\ \rho w V + \eta_z p \\ \rho E V + \eta_{x_i} u_i p \end{bmatrix}$$

$$\boldsymbol{H} = \frac{1}{\mathcal{J}}\begin{bmatrix} \rho W \\ \rho u W + \zeta_x p \\ \rho v W + \zeta_y p \\ \rho w W + \zeta_z p \\ \rho E W + \zeta_{x_i} u_i p \end{bmatrix} \qquad (5)$$

$$\boldsymbol{F}_v = \frac{1}{\mathcal{J}}\begin{bmatrix} 0 \\ \xi_{x_i}\tau_{i1} \\ \xi_{x_i}\tau_{i2} \\ \xi_{x_i}\tau_{i3} \\ \xi_{x_i}(u_j\tau_{ij} - \mathcal{Q}_i) \end{bmatrix}, \qquad \boldsymbol{G}_v = \frac{1}{\mathcal{J}}\begin{bmatrix} 0 \\ \eta_{x_i}\tau_{i1} \\ \eta_{x_i}\tau_{i2} \\ \eta_{x_i}\tau_{i3} \\ \eta_{x_i}(u_j\tau_{ij} - \mathcal{Q}_i) \end{bmatrix}$$

$$\boldsymbol{H}_v = \frac{1}{\mathcal{J}}\begin{bmatrix} 0 \\ \zeta_{x_i}\tau_{i1} \\ \zeta_{x_i}\tau_{i2} \\ \zeta_{x_i}\tau_{i3} \\ \zeta_{x_i}(u_j\tau_{ij} - \mathcal{Q}_i) \end{bmatrix} \qquad (6)$$

where

$$U = \xi_t + \xi_{x_i}u_i, \qquad V = \eta_t + \eta_{x_i}u_i, \qquad W = \zeta_t + \zeta_{x_i}u_i \qquad (7)$$

and

$$E = \frac{T}{\gamma(\gamma - 1)M_\infty^2} + \frac{1}{2}(u^2 + v^2 + w^2) \qquad (8)$$

In the preceding expressions, $u$, $v$, and $w$ are the Cartesian velocity components; $\rho$ is the density; $p$ is the pressure; and $T$ is the

temperature. All length scales have been nondimensionalized by the reference length $r$, and dependent variables have been normalized by their reference values, except for $p$, which has been nondimensionalized by $\rho_\infty q_\infty^2$. Components of the stress tensor and heat flux vector are expressed as

$$\mathcal{Q}_i = -\left[\frac{1}{(\gamma - 1)M_\infty^2}\right]\left(\frac{\mu}{Pr}\right)\frac{\partial \xi_j}{\partial x_i}\frac{\partial T}{\partial \xi_j} \qquad (9)$$

$$\tau_{ij} = \mu\left(\frac{\partial \xi_k}{\partial x_j}\frac{\partial u_i}{\partial \xi_k} + \frac{\partial \xi_k}{\partial x_i}\frac{\partial u_j}{\partial \xi_k} - \frac{2}{3}\delta_{ij}\frac{\partial \xi_l}{\partial x_k}\frac{\partial u_k}{\partial \xi_l}\right) \qquad (10)$$

The Sutherland law for the molecular viscosity coefficient $\mu$ and the perfect-gas relationship,

$$p = \frac{\rho T}{\gamma M_\infty^2} \qquad (11)$$

were also employed, and the Stokes hypothesis for the bulk viscosity coefficient has been invoked.

## IV. Numerical Method for the DNS

Time-accurate solutions to Eq. (3) were obtained numerically by the implicit approximately factored finite difference algorithm of Beam and Warming [38] employing Newton-like subiterations [39], which has evolved as an efficient tool for generating solutions to a wide variety of complex fluid flow problems and may be written as follows:

$$\left[\frac{1}{\mathcal{J}} + \left(\frac{2\Delta t}{3}\right)\delta_{\xi 2}\left(\frac{\partial \boldsymbol{F}^p}{\partial \boldsymbol{Q}} - \frac{1}{Re}\frac{\partial \boldsymbol{F}_v^p}{\partial \boldsymbol{Q}}\right)\right]\mathcal{J} \times \left[\frac{1}{\mathcal{J}} + \left(\frac{2\Delta t}{3}\right)\delta_{\eta 2}\left(\frac{\partial \boldsymbol{G}^p}{\partial \boldsymbol{Q}}\right.\right.$$
$$\left.\left. - \frac{1}{Re}\frac{\partial \boldsymbol{G}_v^p}{\partial \boldsymbol{Q}}\right)\right]\mathcal{J} \times \left[\frac{1}{\mathcal{J}} + \left(\frac{2\Delta t}{3}\right)\delta_{\zeta 2}\left(\frac{\partial \boldsymbol{H}^p}{\partial \boldsymbol{Q}} - \frac{1}{Re}\frac{\partial \boldsymbol{H}_v^p}{\partial \boldsymbol{Q}}\right)\right]\Delta \boldsymbol{Q}$$
$$= -\left(\frac{2\Delta t}{3}\right)\left[\left(\frac{1}{2\Delta t}\right)\left(\frac{3\boldsymbol{Q}^p - 4\boldsymbol{Q}^n + \boldsymbol{Q}^{n-1}}{\mathcal{J}}\right) + \delta_{\xi 6}\left(\boldsymbol{F}^p\right.\right.$$
$$\left.\left. - \frac{1}{Re}\boldsymbol{F}_v^p\right) + \delta_{\eta 6}\left(\boldsymbol{G}^p - \frac{1}{Re}\boldsymbol{G}_v^p\right) + \delta_{\zeta 6}\left(\boldsymbol{H}^p - \frac{1}{Re}\boldsymbol{H}_v^p\right)\right] \qquad (12)$$

In this expression, which is employed to advance the solution in time, $\boldsymbol{Q}^{p+1}$ is the $p + 1$ approximation to $\boldsymbol{Q}$ at the $n + 1$ time level $\boldsymbol{Q}^{n+1}$, and $\Delta \boldsymbol{Q} = \boldsymbol{Q}^{p+1} - \boldsymbol{Q}^p$. For $p = 1$, $\boldsymbol{Q}^p = \boldsymbol{Q}^n$. Second-order-accurate backward-implicit time differencing was used to obtain temporal derivatives.

The implicit segment of the algorithm [left-hand side of Eq. (12)] incorporates second-order-accurate centered differencing for all spatial derivatives and uses nonlinear artificial dissipation [40] to augment stability. Efficiency is enhanced by solving this implicit portion of the factorized equations in diagonalized form [41]. Temporal accuracy, which can be degraded by use of the diagonal form, is maintained by using subiterations within a time step. This technique has been commonly invoked in order to reduce errors due to factorization, linearization, diagonalization, and explicit application of boundary conditions. It is useful for achieving temporal accuracy on overset zonal mesh systems and for a domain decomposition implementation on parallel computing platforms. Any deterioration of the solution caused by use of artificial dissipation and by lower-order spatial resolution of implicit operators is also reduced by the procedure. Three subiterations per time step have been applied in the current simulations to preserve second-order temporal accuracy.

The compact difference scheme employed on the right-hand side of Eq. (12) is based upon the pentadiagonal system of Lele [42] and is capable of attaining spectral-like resolution. This is achieved through the use of a centered implicit difference operator with a compact stencil, thereby reducing the associated discretization error. For the present computations, a sixth-order tridiagonal subset of Lele's system is used, which is illustrated here in one spatial dimension as

$$\alpha \left( \frac{\partial \boldsymbol{F}}{\partial \xi} \right)_{i-1} + \left( \frac{\partial \boldsymbol{F}}{\partial \xi} \right)_{i} + \alpha \left( \frac{\partial \boldsymbol{F}}{\partial \xi} \right)_{i+1} = a \left( \frac{\boldsymbol{F}_{i+1} - \boldsymbol{F}_{i-1}}{2} \right)$$
$$+ b \left( \frac{\boldsymbol{F}_{i+2} - \boldsymbol{F}_{i-2}}{4} \right) \tag{13}$$

with $\alpha = 1/3$, $a = 14/9$, and $b = 1/9$. The scheme has been adapted by Visbal and Gaitonde [43] as an implicit iterative time-marching technique, applicable for unsteady vortical flows, and has been used to obtain the spatial derivative of any scalar, flow variable, metric coefficient, or flux component. It is used in conjunction with a low-pass Padé-type nondispersive spatial filter developed by Gaitonde et al. [44], which has been shown to be superior to the use of explicitly added artificial dissipation for maintaining both stability and accuracy on stretched curvilinear meshes [43]. The filter is applied to the solution vector sequentially in each of the three computational directions following each subiteration and is implemented in one dimension as

$$\alpha_f \hat{\boldsymbol{Q}}_{i-1} + \hat{\boldsymbol{Q}}_i + \alpha_f \hat{\boldsymbol{Q}}_{i+1} = \sum_{n=0}^{4} \frac{a_n}{2} (\boldsymbol{Q}_{i+n} + \boldsymbol{Q}_{i-n}) \tag{14}$$

where $\hat{\boldsymbol{Q}}$ designates the filtered value of $\boldsymbol{Q}$. It is noted that the filtering operation is a postprocessing technique, applied to the evolving solution in order to regularize features that are captured but poorly resolved. Equation (14) represents a one-parameter family of eighth-order filters, where numerical values for the $a_n$ may be found in [45]. The filter coefficient $\alpha_f$ is a free adjustable parameter that may be selected for specific applications and has been set to 0.40 for the present simulations.

The aforementioned features of the numerical algorithm are embodied in a parallel version of the time-accurate three-dimensional computer code FDL3DI [45], which has proven to be reliable for steady and unsteady fluid flow problems, including vortex breakdown [46,47], transitional wall jets [48], synthetic jet actuators [49], roughness elements [50], plasma flows [51–56], and direct numerical and large-eddy simulations of subsonic [57,58] and supersonic flowfields [59,60].

## V. Stability Analysis

Challenges of the present computations for swept-wing flows in flight are related to the strongly nonlinear nature of the crossflow instability, along with ultrasensitivity to leading-edge micron-sized roughness elements. The traditional approach to predicting transition in design applications is predicated upon linear stability analysis and uses the $e^N$ methodology. The quantity $N$ is obtained by integrating the linear growth rate from the first neutrally stable point to a location somewhere downstream on the body. Because $e^N$ represents only an amplitude ratio, $N$ must be correlated with an experimentally determined transition Reynolds number for a variety of observations. This correlation will produce a value for $N$, which can then be taken as a transition criterion and used to predict the transition Reynolds number for cases in which experimental data are not available.

The role of receptivity, not accounted for in linear stability theory, is key to the overall transition process, as it defines the initial disturbance amplitude. Moreover, the transition process for crossflow has been shown to be nonlinear. Linear stability theory (without curvature) serves to predict the most unstable wavelengths and very early growth, but does not capture the physics of the breakdown process. One of the most promising numerical approaches for modern transition prediction is the nonlinear parabolized stability equation formulation. Details, formulations, and critiques relative to applications of this approach are found in [61].

## VI. Governing Equations for the NPSE

In recent years, the nonlinear parabolized stability equation formulation has become a popular approach for stability analysis, due to the inclusion of nonparallel, curvature, and nonlinear effects. Resource requirements as compared with direct numerical simulation are

relatively small [62]. For NPSE, every disturbance quantity is transformed spectrally in the spanwise direction and temporally. Each mode $n$ and $k$ is the product of a slowly varying shape function and a rapidly varying wave function. Streamwise second-derivative terms on the order of $1/R_0^2$ are neglected in the governing equations. The resulting system is parabolic, so to complete the formulation, upstream (initial) and boundary conditions must be specified. If the analysis begins in a region where the initial disturbance amplitudes are small, linear stability theory can be used to obtain the initial conditions.

The NPSE formulation uses a body-intrinsic coordinate system and the curvature is included in the associated metric coefficients. For most cases, the inclusion of curvature has a very small effect on the metric coefficients. With an airfoil shape, the maximum values occur in the first few percent of chord, where the inverse of the radius of curvature is typically on the order of 0.01 to 0.001. This generally decreases sharply with increasing chordwise distance. Because of this, many researchers have neglected curvature, but the work of Haynes and Reed [24] demonstrated conclusively that small changes in the metric coefficients can have a significant effect on the development of instabilities. Typically, convex curvature is stabilizing and nonparallel effects are destabilizing. The two effects tend to balance each other, such that the proper formulation is to neglect curvature in linear stability theory. On the other hand, concave curvature is highly destabilizing to Görtler instabilities on concave walls [63]. In the present investigation, curvature is explicitly accounted for with the NPSE formulation.

The use of the NPSE is hampered by a lack of knowledge connecting the freestream, the surface roughness, and the boundary-layer response. A physically appropriate upstream condition must be specified. However, the NPSE have been demonstrated to accurately model the transition process for a wide variety of convective flows, including crossflow, when the environment and operating conditions are modeled correctly [61].

The nonlinear parabolized stability equations are obtained by separating the flow variables into a steady basic state and unsteady disturbance quantities as

$$\boldsymbol{\phi}\left( \xi_s, \eta_s, \zeta_s, \tau \right) = \boldsymbol{\Phi}(\xi_s, \eta_s, \zeta_s) + \boldsymbol{\phi}'(\xi_s, \eta_s, \zeta_s, \tau) \tag{15}$$

where

$$\boldsymbol{\phi} = [\, \rho \quad u \quad v \quad w \quad T \,]^T \quad \text{and} \quad \boldsymbol{\phi}' = [\, \rho' \quad u' \quad v' \quad w' \quad T' \,]^T \tag{16}$$

Here, $\xi_s$, $\eta_s$, and $\zeta_s$ are body-intrinsic orthogonal curvilinear coordinates, and $\boldsymbol{\Phi}$ is obtained from the DNS. Equation (15) is then substituted into the Navier–Stokes equations, and the portion of the resulting expression that is satisfied by $\boldsymbol{\Phi}$ is subtracted to arrive at the following form:

$$\mathcal{B}_0 \frac{\partial \boldsymbol{\phi}'}{\partial \tau} + \mathcal{B}_1 \frac{\partial \boldsymbol{\phi}'}{\partial \xi_s} + \mathcal{B}_2 \frac{\partial \boldsymbol{\phi}'}{\partial \eta_s} + \mathcal{B}_3 \frac{\partial \boldsymbol{\phi}'}{\partial \zeta_s} + \mathcal{C}_1 \frac{\partial^2 \boldsymbol{\phi}'}{\partial \xi_s^2} + \mathcal{C}_2 \frac{\partial^2 \boldsymbol{\phi}'}{\partial \eta_s^2}$$
$$+ \mathcal{C}_3 \frac{\partial^2 \boldsymbol{\phi}'}{\partial \zeta_s^2} + \mathcal{D}_1 \frac{\partial^2 \boldsymbol{\phi}'}{\partial \xi_s \partial \eta_s} + \mathcal{D}_2 \frac{\partial^2 \boldsymbol{\phi}'}{\partial \xi_s \partial \zeta_s} + \mathcal{D}_3 \frac{\partial^2 \boldsymbol{\phi}'}{\partial \eta_s \partial \zeta_s}$$
$$+ \mathcal{D}_4 \boldsymbol{\phi}' = \mathcal{N} \tag{17}$$

Elements of the coefficient matrices $\mathcal{B}_i$, $\mathcal{C}_i$, and $\mathcal{D}_i$ and the right-hand side $\mathcal{N}$ are given in [64]. Complete details of solving the equations are found in [24,64], which are only briefly summarized here. The disturbance vector $\boldsymbol{\phi}'$ is transformed spectrally in the spanwise direction and temporally according to

$$\boldsymbol{\phi}'(\xi_s, \eta_s, \zeta_s, \tau) = \sum_{n=-\infty}^{+\infty} \sum_{k=-\infty}^{+\infty} \tilde{\boldsymbol{\phi}}_{n,k}(\bar{\xi}_s, \eta_s) \mathcal{A}_{n,k}(\xi_s) e^{i(k\beta_0 \zeta_s - n\omega_0 \tau)} \tag{18}$$

where $\tilde{\boldsymbol{\phi}}_{n,k}(\bar{\xi}_s, \eta_s)$ is a shape function, $\mathcal{A}_{n,k}(\xi_s) e^{i(k\beta_0 \zeta_s - n\omega_0 \tau)}$ is a planar wave function, and

$$\frac{\mathrm{d}\mathcal{A}_{n,k}}{\mathrm{d}\xi_s} = \mathcal{A}_{n,k} i\alpha_{n,k}(\bar{\xi}_s) \tag{19}$$

In the above, $\omega_0$ and $\beta_0$ are the fundamental temporal frequency and spanwise wave number of the disturbance, respectively, $\mathcal{A}_{n,k}$ is the modal wave number amplitude, $\alpha_{n,k}$ is the modal streamwise wave number, and $\xi_s$ has been scaled as

$$\xi_s = R_0\bar{\xi}_s, \qquad R_0 = \rho_\infty q_\infty \delta_0/\mu_\infty \tag{20}$$

The spectral expansion of the disturbance vector allows Eq. (17) to be expressed as

$$\sum_{n=-\infty}^{+\infty} \sum_{k=-\infty}^{+\infty} \left[ (\mathcal{L}_0 + \mathcal{L}_1)\tilde{\boldsymbol{\phi}}_{n,k} + \mathcal{L}_2 \frac{\partial\tilde{\boldsymbol{\phi}}_{n,k}}{\partial\bar{\xi}_s} \right.$$
$$\left. + \frac{\mathrm{d}\alpha_{n,k}}{\mathrm{d}\bar{\xi}_s} \mathcal{L}_3\tilde{\boldsymbol{\phi}}_{n,k} \right] \mathcal{A}_{n,k} e^{i(k\beta_0\zeta_s - n\omega_0\tau)} = \mathcal{N} \tag{21}$$

Equation (21) is now parabolic, and the solution for $\tilde{\boldsymbol{\phi}}_{n,k}$ can be obtained by spatial marching. The operational matrices $\mathcal{L}_i$ are provided in [64]. A second-order-accurate backward Euler scheme was used to obtain solutions to the equation, where a fourth-order-accurate finite difference approximation was applied to form derivatives in the wall-normal direction. Each mode is required to satisfy a normalization constraint, which is described in [24,64] along with the appropriate boundary conditions. Bertolotti and Joslin [65] discuss the effects of far-field boundary conditions on boundary-layer transition. For the present investigation of crossflow on a swept wing in flight, the instability will be stationary so that the frequency is assumed to be zero.

## VII. Baseline Computations of the SWIFT Model

As previously noted, flight-test experiments were conducted for the SWIFT model. These experiments were carried out on a Cessna O-2A Skymaster aircraft at a chord-based Reynolds number of $7.4 \times 10^6$. The Skymaster aircraft is indicated in Fig. 5a. Various leading-edge discrete roughness configurations were correlated with local skin-friction measurements [15,16]. As a companion to the flight experiments, the goal of the present work is to provide a computational study that relates features of the roughness elements to the resulting initial amplitude of the instability. This will provide a critical connection between stability analysis design methods and transition location prediction.

As part of the SWIFT investigation, a complete-aircraft mean flow computation was carried out, based upon solution of the laminar Navier–Stokes equations [66,67]. Shown in Fig. 5b is the surface grid geometry employed for the SWIFT calculations. Results of these computations also helped validate the flight-test configuration and operating conditions. Physical limitations restricted placement of data probes during flight; therefore, the SWIFT computations were needed to quantify influence of the aircraft on the SWIFT model.

To obtain a baseline solution for the mean flow about the Cessna aircraft and SWIFT configuration, a simplified solid model was created using commercial software. It was determined that the tail assembly, starboard boom, and starboard strut were located far enough away from the area of interest that they could be neglected. The region under the port wing (including the SWIFT model and its mount) was completely reconstructed using measurements taken directly from the aircraft. The resulting solid model was then used to create a computational mesh about the Cessna aircraft. A laminar Navier–Stokes solution was obtained from commercially available software. Grid convergence and other studies were performed as part of the investigation. Surface pressure coefficient distributions from the computations and from experimental measurements are displayed in Fig. 6. Results along the inboard portion of the model appear in the figure. The baseline SWIFT computations can be used in conjunction with perturbations obtained from the DNS to conduct stability calculations carried out with the NPSE.



a)
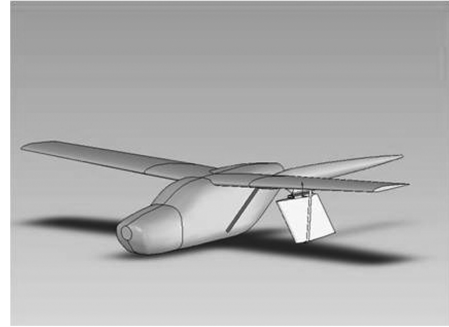


b)

Fig. 5 Cessna O-2A Skymaster experimental flight configuration: a) Cessna O-2A Skymaster aircraft and b) surface geometry for SWIFT computations.
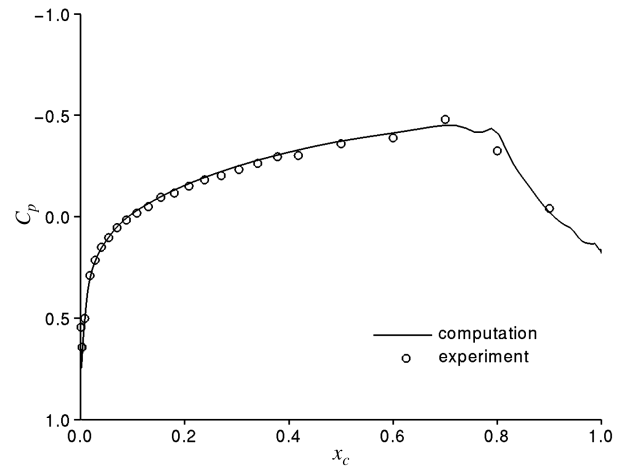


Fig. 6 Comparison of SWIFT model surface pressure coefficient computations with experimental measurements.

## VIII. Results of the DNS

Computations of all DNS were carried out with a time step of $\Delta t = 0.0005$, which was dictated by stability requirements. Although the solutions were temporally accurate, each converged to steady state, including those for roughness elements. In addition to the $1061 \times 301 \times 121$ mesh system for the baseline flow about the parabolic cylinder, a coarser grid was constructed by removing every other mesh point in each coordinate direction. For the purposes of comparison only, these two systems will be referred to as the fine and coarse grids, respectively. In all other cases, results will correspond to solutions obtained on the finer mesh. Velocity contours in the leading-edge region on the two grid systems are provided in Fig. 7. In this view, only slight differences are observed between the two solutions. A more quantitative comparison is illustrated by the
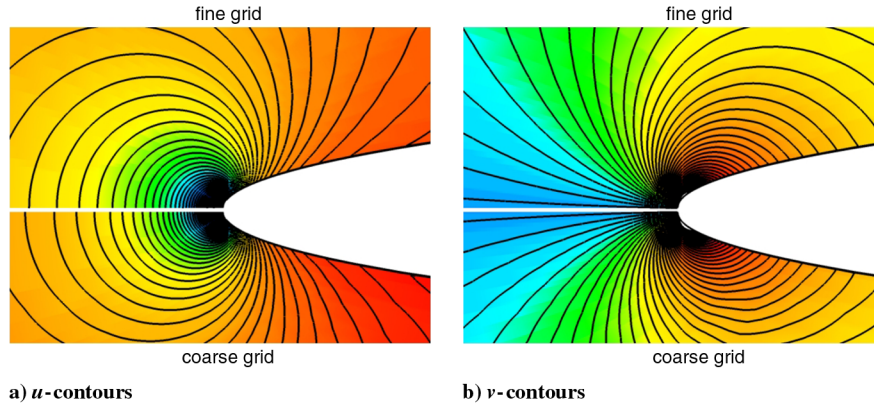
a) *u*-contours                                    b) *v*-contours

**Fig. 7    Planar contours and contour lines of velocity for the baseline flow on the fine and coarse computational meshes: a) *u* velocity component and b) *v* velocity component.**

velocity profiles in Figs. 8 and 9. For these figures, the local boundary-layer thickness $\delta$ corresponds to the normal distance from the surface, where the spanwise velocity $w$ attains 0.99% of its freestream value. This same criterion was employed by Collis and Lele [21]. Edge values of the velocity components $(u_e, w_e)$ were evaluated at the same location. On the fine computational grid, 162 points in the wall-normal direction were within the boundary layer. The streamwise value $x = 0.79$ in the figures corresponds to the center location of the roughness elements in the perturbed flows. The other streamwise location $x = 1.58$ is twice as far as the element is from the leading edge. We note that the coarse grid has only one-eighth of the number of mesh points of that of the fine grid. The small variations between the respective solutions tend to indicate that resolution on the fine grid is adequate. Because the roughness elements are so small, no alternate grids were considered for roughness simulations.

Shown in Fig. 10 is the surface pressure coefficient distribution for the baseline flow over the parabolic cylinder, which is compared with the computation and experimental data of the SWIFT model. Note that the angle of attack for the parabolic cylinder is 0 deg, while that of the SWIFT model is $-4.69$. Despite that difference, the DNS produces a reasonable representation of the flight situation. Figure 11 exhibits streamlines of the flow over roughness elements for a height $h = 20~\mu$m. Because the elements are so thin and the speed of the flow near the parabola surface is low, the streamlines are only slightly deflected by the presence of the elements. There is no evidence of a horseshoe vortex produced upstream of the elements, as would occur if the height were considerably larger.

Solutions of DNS from the baseline flow were subtracted from the roughness DNS to create perturbation flowfields. The kinetic energy from the perturbation flow is represented in the form of planar

contours in Fig. 12. To enhance visualization of the region close to the parabola surface, planes in the figure were stretched by a factor of 6 in the vertical direction. As would be expected, the largest element (cylinder $h = 30~\mu$m) produces the largest kinetic energy. The square element generates more energy than the cylindrical element of the same height. This is not only because the volume of the element is larger, but also because it has sharp vertical edges that are absent in the other configurations. The smooth bump with $h = 20~\mu$m generates more energy than the cylinder with $h = 10~\mu$m, but less than the cylinder with $h = 20~\mu$m. The smooth bump has only


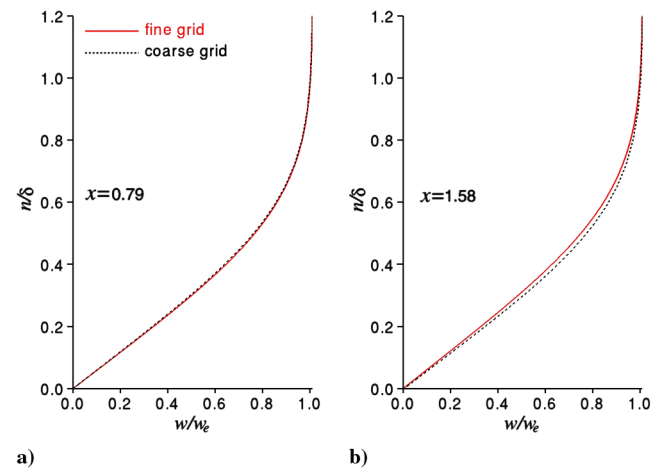
a)                                                    b)

**Fig. 9    Profiles of the *w* velocity component for the baseline flow on the fine and coarse computational meshes: a) $x = 0.79$ and b) $x = 1.58$.**
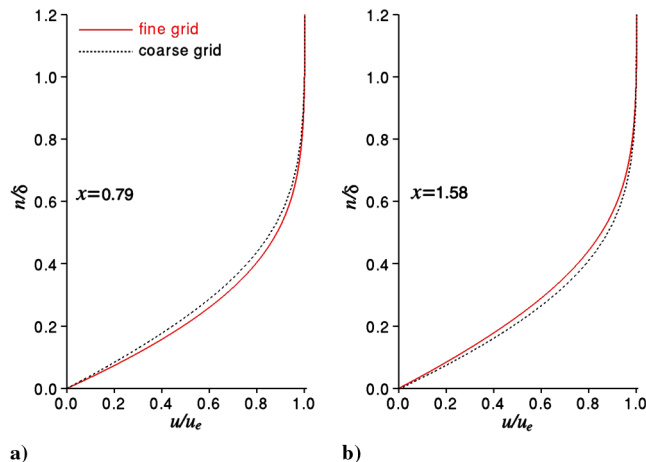


a)                                                    b)

**Fig. 8    Profiles of the *u* velocity component for the baseline flow on the fine and coarse computational meshes: a) $x = 0.79$ and b) $x = 1.58$.**
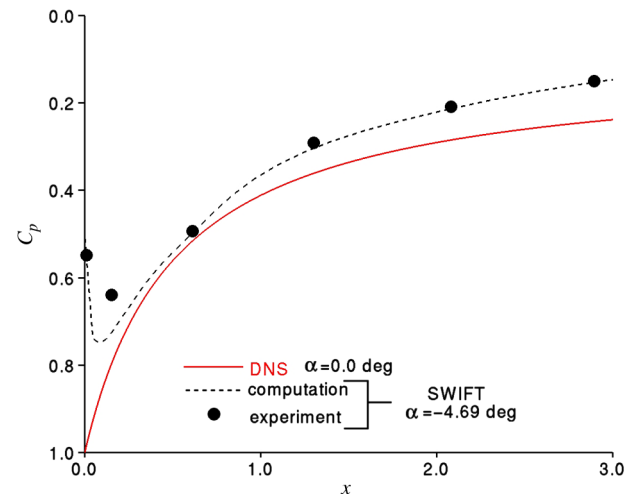


**Fig. 10    Surface pressure coefficient distributions of the baseline flow.**
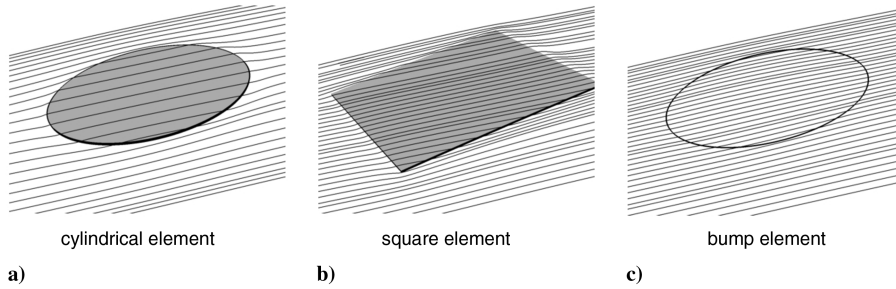
**Fig. 11 Streamlines of the flow over roughness elements for $h = 20$ $\mu$m: a) cylindrical element, b) square element, and c) bump element.**

one-half of the volume of that of a cylindrical element with the same height.

A more quantitative representation of the perturbation kinetic energy was obtained by integrating this quantity over a computational plane and plotting the resulting value as a function of streamwise distance. That result is given in Fig. 13a. The previously described behavior with regard to the shape and size of the roughness elements is apparent in the figure. In all cases, the energy declines rapidly beyond $x \approx 3.5$, because the grid begins to coarsen and is unable to sustain sufficient resolution to capture the very weak structures. Because of the observed behavior in Fig. 13a, it was conjectured that a simple scaling might reduce the integrated energy to a universal form. To test this concept, the following scaled perturbation kinetic energy $k_s$ was defined:

$$k_s = \left(\frac{h}{h_r}\right)\left(\frac{\text{volume}}{\text{volume}_r}\right)k \qquad (22)$$

For the above expression, reference quantities for the height and elemental volume are taken as those of the cylindrical element with $h = 20$ $\mu$m. The scaled perturbation energy distributions appear in Fig. 13b. As is evident in the figure, Eq. (22) works reasonably well for the cylindrical elements, but not for the other shapes. It appears that the proposed scaling may be appropriate only for a single family of shapes. To achieve a general universal scaling law, a more sophisticated expression than the simple relationship provided in Eq. (22) might be required.

Shown in Fig. 14 are the steady crossflow vortices that evolve in the roughness-element flowfields. These are represented as isosurfaces of the perturbation kinetic energy that have been colored by the streamwise component of velocity ($u$). The depictions depend
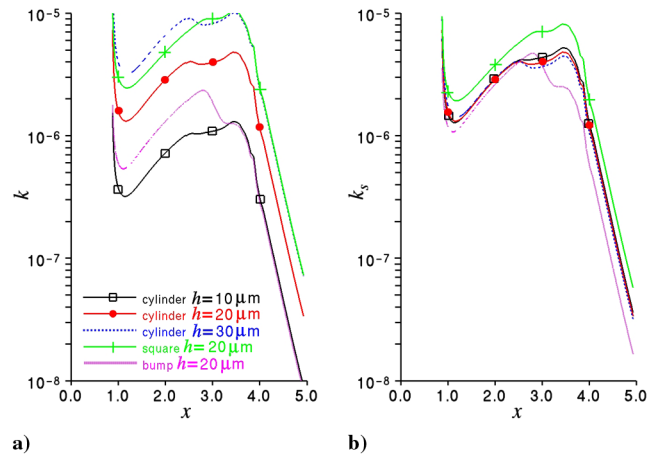


**Fig. 13 Planar integrated perturbation kinetic energy distributions: a) unscaled distribution and b) scaled distribution.**

to a certain extent upon the level of the isosurface chosen in each case. The arrangements of the vortical structures are somewhat irregular. This is because some of the vortices are primary structures generated by the roughness elements and some are secondary structures induced by the primary ones.

Figure 15 exhibits contours of the perturbation vorticity component that is normal to the axis of the crossflow vortices. In this figure, the direction normal to the parabola surface has been stretched by a factor of 10 to enhance visualization. Consistent with Fig. 14, the alternating sense of the vorticity component (positive or negative)
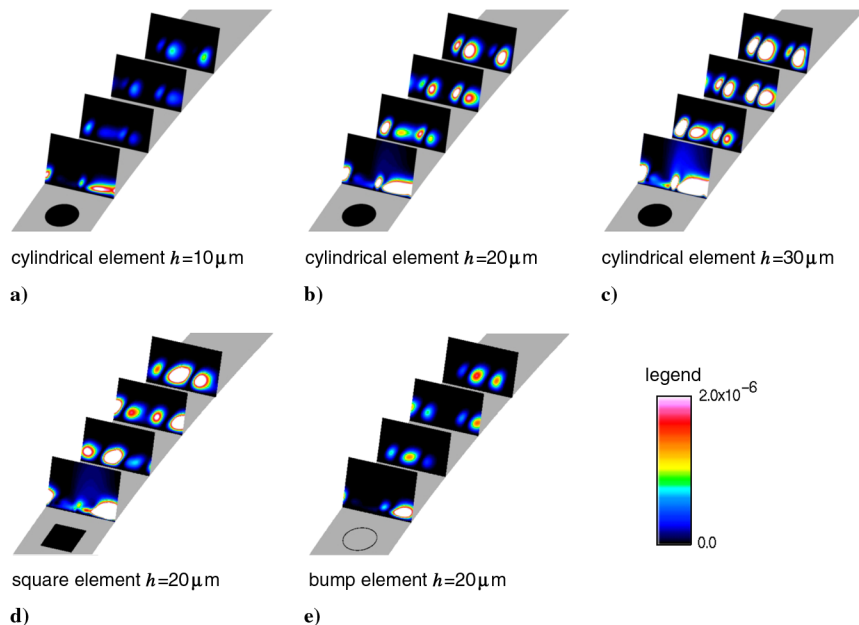


**Fig. 12 Contours of perturbation kinetic energy: a) cylindrical element $h = 10$ $\mu$m, b) cylindrical element $h = 20$ $\mu$m, c) cylindrical element $h = 30$ $\mu$m, d) square element $h = 20$ $\mu$m, and e) bump element $h = 20$ $\mu$m.**
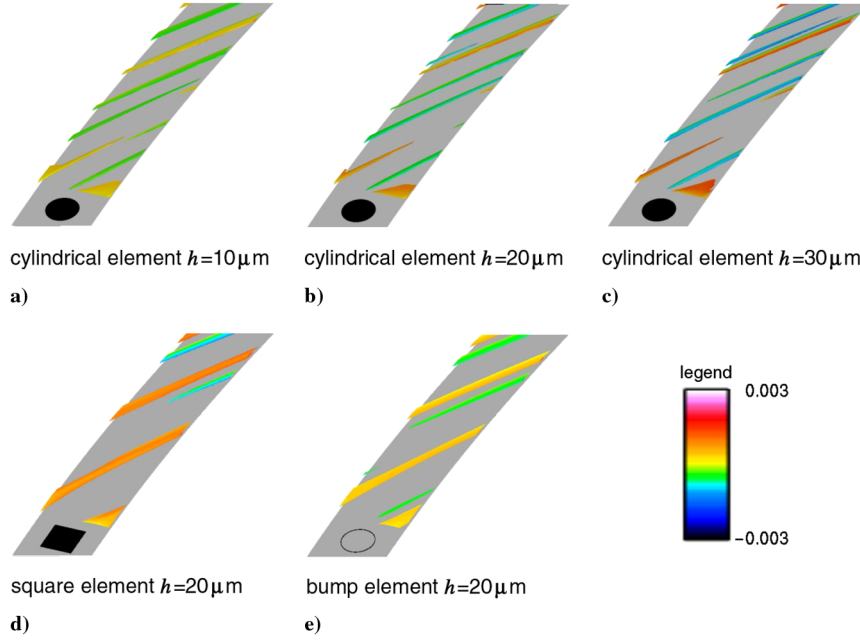
Fig. 14  Isosurfaces of perturbation kinetic energy colored by $u$ velocity: a) cylindrical element $h = 10$ $\mu$m, b) cylindrical element $h = 20$ $\mu$m, c) cylindrical element $h = 30$ $\mu$m, d) square element $h = 20$ $\mu$m, and e) bump element $h = 20$ $\mu$m.
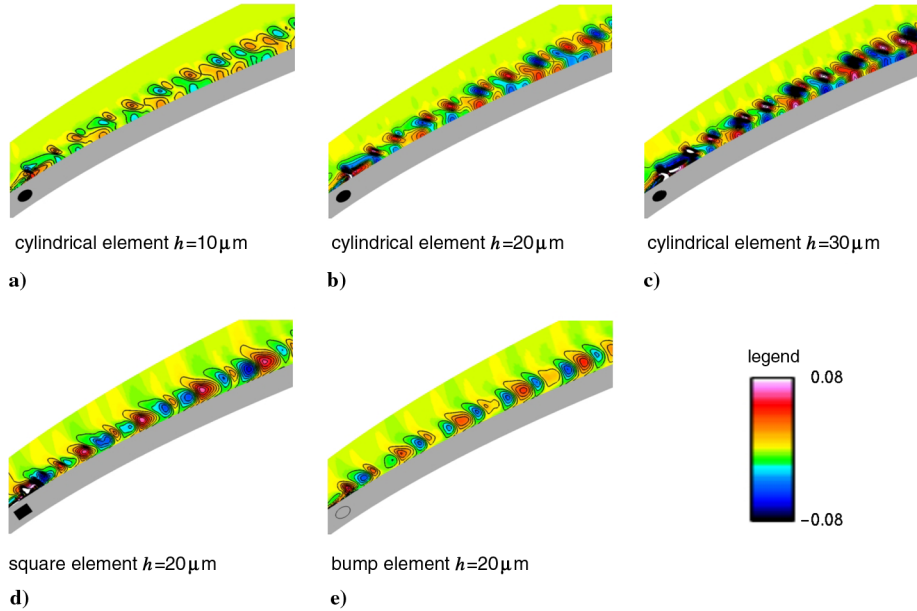


Fig. 15  Planar contours of perturbation vorticity component normal to axis of crossflow vortices: a) cylindrical element $h = 10$ $\mu$m, b) cylindrical element $h = 20$ $\mu$m, c) cylindrical element $h = 30$ $\mu$m, d) square element $h = 20$ $\mu$m, and e) bump element $h = 20$ $\mu$m. (normal direction stretch by factor of 10).

reflects the generation of primary or secondary structures. The cylindrical elements have identical vorticity patterns for all heights, although the vorticity magnitude increases with increasing height. The square element produces a slightly different pattern, which lacks induced vorticity in the near-wall region. The bump element generates a pattern similar to that of the square element, with a lower magnitude.

## IX.   Results of the NPSE

The NPSE are applied by assuming that critical stationary crossflow disturbances are generated by the spanwise-periodic discrete roughness elements at flight conditions. Thus, the fundamental temporal frequency $\omega_0 = 0$. In addition, Reibert et al. [68] found that the discrete roughness elements generate only unstable

waves at integer multiples of the physical roughness wave number. No intermediate or subharmonics appear. Therefore, the fundamental spanwise wave number $\beta_0$ corresponds to the wavelength of the most unstable stationary crossflow mode for the SWIFT model (0.0045 m).

In this effort, roughness spectra (amplitude and phase) determined from the DNS at the location $x_c = 0.02$ were applied as initial conditions to the NPSE. These were used to evaluate the evolution of stationary crossflow disturbances on both the DNS of the parabolic leading edge and of the computed solution of the SWIFT flowfield. Results of the calculations are found in figures to follow. Initial spatial spanwise frequency spectra of the maximum $u_t'$ values as predicted by the DNS are given in Fig. 16. These spectra were collected at the initial upstream location $x_c = 0.02$, along a line at a fixed normal distance from the parabola surface where the maximum
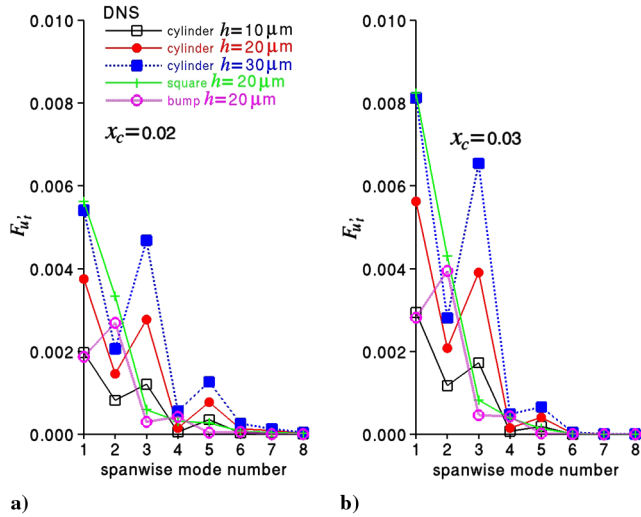
a)

b)

**Fig. 16  Initial spatial spanwise frequency spectra of the maximum tangential velocity perturbation for all roughness elements: a) $x_c = 0.02$ and b) $x_c = 0.03$.**

in $u'_t$ occurred for each mode. In Fig. 16 and some figures to follow, the tangential disturbance velocity has been normalized by its edge value at $x_c = 0.02$. Figure 16a shows results at $x_c = 0.02$, and those at $x_c = 0.03$ are given in Fig. 16b. The first mode corresponds to the fundamental interelement spacing $\lambda$. For all cylindrical elements, the first mode provides the largest contribution to the spectra, but the third mode is also significant. In the case of the square element, the second mode is appreciable. For the bump element, the second mode is dominant. These results indicate that the initial spanwise spectral content is highly dependent upon the shape of roughness elements. It can be observed in Fig. 16b that amplitudes for all of the first three modes increase downstream, while amplitudes of the higher modes decay.

In all of the stability calculations to follow, solutions were obtained using both 16 and 32 spanwise modes that were initiated from the DNS. Results of those calculations were indistinguishable from each other.

Shown in Fig. 17 are the initial spanwise frequency spectra of the cylindrical elements, where the amplitude of each mode has been normalized by the corresponding amplitude of the $h = 10$ $\mu$m result. Thus, for the case of $h = 10$ $\mu$m, all the normalized amplitudes are identically equal to 1.0. If the amplitudes varied linearly with element height, then the normalized values for $h = 20$ and 30 $\mu$m would be

2.0 and 3.0, respectively. The figure emphasizes the fact that the initial growth of the crossflow structures is a nonlinear function of the elemental height. This result does not contradict the previous finding of Eq. (22) and Fig. 13, in which a linear dependence on $h$ was found for the perturbation kinetic energy, as the energy is an integrated quantity. Spectra for modes higher than four are not shown in the figure, as those are decaying and the normalization produces artificially high values.

For subsequent figures, the following designations are employed:
1) DNS refers to the present DNS including the roughness elements.
2) DNS/NPSE implies that the mean flow is provided by the present DNS for the baseline flow about the parabolic cylinder without roughness and the DNS with roughness are used to provide initial conditions and spectra to the NPSE, which are then marched downstream.
3) SWIFT/NPSE indicates that the mean flow is the computed solution of the SWIFT model and the DNS with roughness are used to provide initial conditions and spectra to the NPSE, which are then marched downstream.

Disturbance velocity profiles at $x_c = 0.03$ for the cylindrical element with $h = 20$ $\mu$m are compared for the DNS and DNS/NPSE calculations in Fig. 18. Streamwise velocity components $u'$ appear in Fig. 18a, and spanwise components $w'$ appear in Fig. 18b. Correspondence of the profiles from the respective calculations serves as a validation of the DNS/NPSE approach to recover the DNS solution.

Figure 19 displays the initial evolution for the amplitude of the maximum tangential velocity perturbation $u'_t$ and the $N$ factor resulting from the DNS/NPSE calculation for all roughness elements. It is illustrated in Fig. 19a that different roughness shapes lead to different initial amplitude growth, as could have been anticipated. Here, and in results to follow, the initial amplitude corresponds to the maximum value along a distance normal to the surface at the upstream location $x_c = 0.02$. The shortest (cylinder $h = 10$ $\mu$m) and tallest (cylinder $h = 30$ $\mu$m) elements have the smallest and largest amplitudes, respectively. We point out that although the bump element is taller than the cylindrical with $h = 10$ $\mu$m, the volume of each is identical. The square element has approximately 85% of the volume of that of the cylindrical element with $h = 30$ $\mu$m. Because of the amplitude ratio and logarithmic nature of the $N$ factor, very little dependence upon element shape or height is evident in Fig. 19b.

The initial evolution of the velocity amplitude and $N$ factor for cylindrical roughness elements, as predicted by the DNS, DNS/NPSE, and SWIFT/NPSE calculations are found in Fig. 20. Results for the other elements are similar to those shown in the figure, but
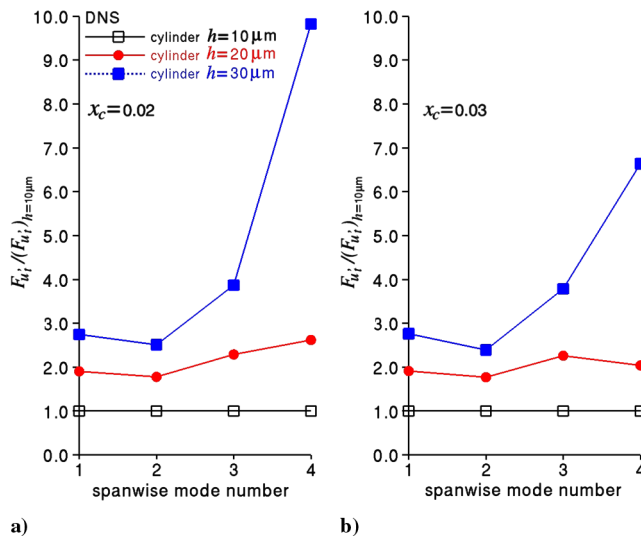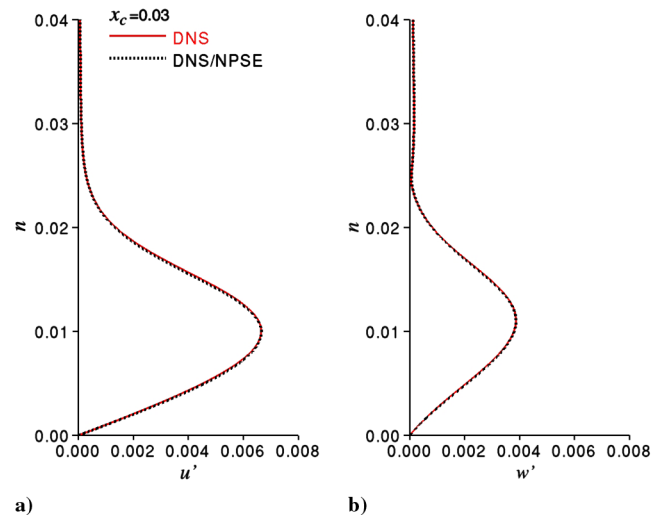


a)

b)

**Fig. 17  Normalized initial spatial spanwise frequency spectra of the maximum tangential velocity perturbation for the cylindrical elements: a) $x_c = 0.02$ and b) $x_c = 0.03$.**



a)

b)

**Fig. 18  Disturbance velocity profiles at $x_c = 0.03$ for the cylindrical element with $h = 20$ $\mu$m predicted by DNS and DNS/NPSE calculations: a) $u'$ velocity component and b) $w'$ velocity component.**

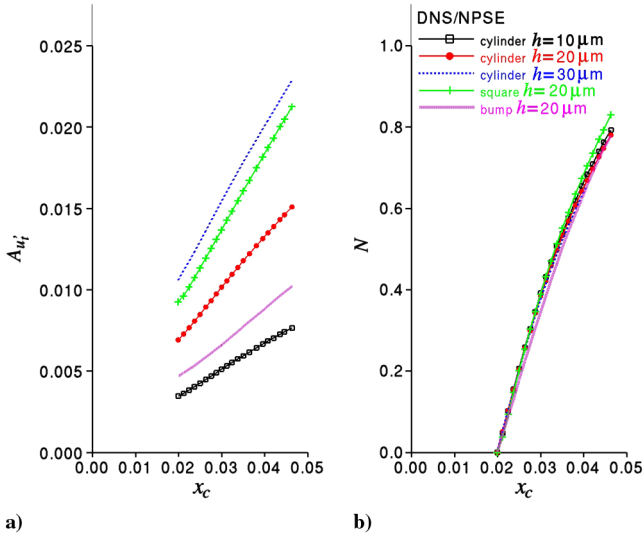**Fig. 19 Initial evolution of crossflow disturbances predicted by DNS/ NPSE calculation for all roughness elements: a) $A_{u'_t}$ and b) $N$ factor.**



**Fig. 21 Downstream evolution of crossflow disturbances predicted by SWIFT/NPSE calculation for all roughness elements: a) $A_{u'_t}$ and b) $N$ factor.**

have been omitted here for clarity. While the variation with elemental height is apparent in Fig. 20a, there is also a well-defined trend with regard to the solution technique. The DNS calculation always produces the smallest amplitude, while the SWIFT/NPSE produces the largest. This seems plausible, as the SWIFT model generated a somewhat stronger pressure gradient (see Fig. 10). For $x_c$ greater than about 0.035, the computational mesh for the DNS begins to coarsen and the amplitude is not captured accurately. This effect was noted previously with the perturbation kinetic energy in Fig. 13. In the early evolution ($x_c \leq 0.03$), the DNS/NPSE solution agrees well with the DNS. The SWIFT/NPSE solution begins to differ from the DNS/ NPSE for increasing $x_c$, because the mean states are not the same.

An important observation in Fig. 20a is that in the early evolution of $A_{u_t}$, the amplitudes predicted by the DNS/NPSE and SWIFT/ NPSE are quite similar. This is true despite that fact that the mean flows from the respective approaches are not the same. Downstream, the differences between the methods should be expected. It may be concluded that for the purposes of a stability analysis, the DNS about the parabolic cylinder is a reasonable approximation to the actual flow past the SWIFT configuration in the leading-edge region, even though the geometry and angle of attack are different. Figure 20b indicates that the $N$ factor is somewhat dependent on the calculation

method for increasing $x_c$ and is relatively insensitive to the element height.

Provided in Fig. 21 are the downstream evolution of the velocity amplitude and $N$ factor. Because the present DNS describes just the leading-edge region, these calculations could only be conducted for the SWIFT/NPSE approach. The solution for each roughness element was carried out up to $x_c = 0.4$. As expected for the cylindrical roughness, the largest element produced the largest $A_{u'_t}$ amplitude. At $x_c = 0.4$, the largest overall amplitude was generated by the square element. The cylindrical element with $h = 10~\mu m$ generally resulted in the smallest amplitude. All elements indicate a nonlinear variation in $x_c$. The nonlinearities create additional modes, which are unique to both the size and shape of specific roughness elements.

The $N$ factors appearing in Fig. 21b exhibit the same initial growth for all roughness elements, as was previously observed in Fig. 19b. It is apparent downstream, however, that different roughness shapes and heights produce different growth rates. This behavior emphasizes the necessity for accurately modeling the geometry of the roughness elements in any receptivity studies. In the region at the end of the computations ($x_c = 0.4$), amplitudes for all elements have grown by several orders of magnitude and may represent the start of transition. In flight tests of the SWIFT model, transition was found to occur at about $x_c = 0.30$ for roughness elements somewhat larger than those considered here.

## X. Conclusions

Direct numerical simulations were carried out for an array of discrete micron-sized roughness elements, which were mounted near the leading edge of a 30 deg swept wing at a chord Reynolds number of $7.4 \times 10^6$. To make the simulations tractable, the geometry was scaled by the wing leading-edge radius and the region of interest was approximated by the flow past an infinite parabolic cylinder. Solutions were obtained by a high-order overset method so that roughness elemental shapes could be accurately represented. The configuration and flow conditions corresponded to an experimental flight test.

An investigation of grid fineness indicated adequacy of the mesh resolution for the baseline flow without roughness. Direct numerical simulations were performed for three different roughness-element shapes: cylindrical, square, and smooth parabolic bump. For cylindrical elements, three different heights were considered. DNS provided detailed solutions of discrete spanwise-periodic roughness elements near the leading edge and was able to capture the generation of crossflow vortices. Characteristics of the perturbation kinetic energy produced by the vortices were elucidated. Disturbances
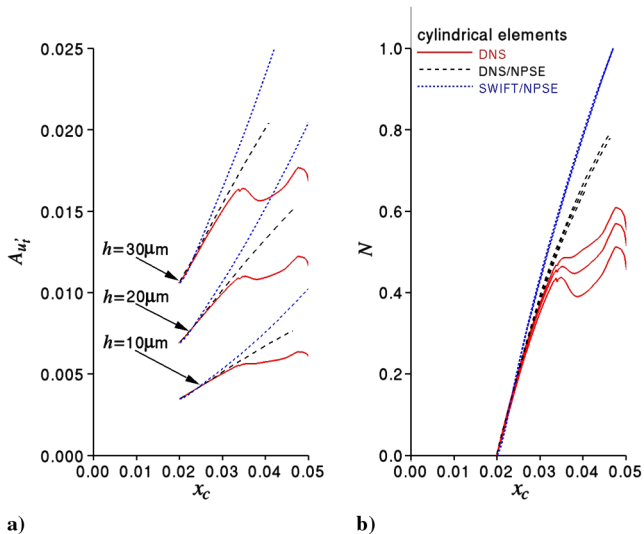


**Fig. 20 Initial evolution of crossflow disturbances predicted by DNS, DNS/NPSE, and SWIFT/NPSE calculation for cylindrical roughness elements: a) $A_{u'_t}$ and b) $N$ factor.**
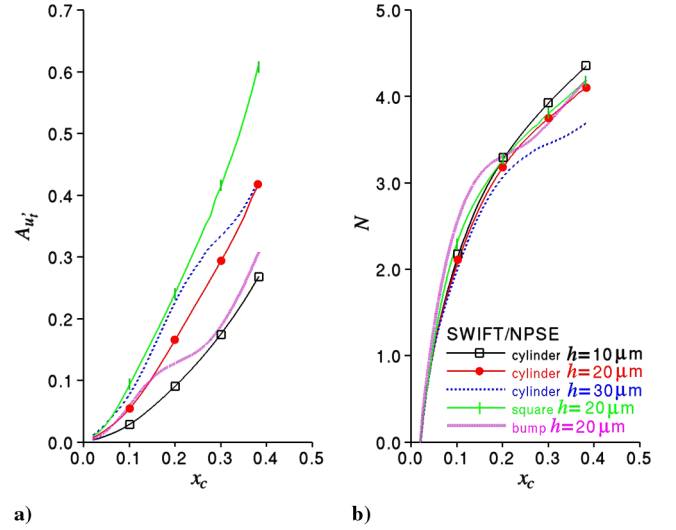
arising from the roughness elements then served as input to a stability analysis that was carried out by solution of the nonlinear parabolized stability equations. Two different stability approaches were considered in the investigation. The mean flow could be supplied by the present DNS for flow about a parabolic leading edge without roughness (DNS/NPSE) or could be obtained from a previous Navier–Stokes calculation about the complete experimental aircraft configuration (SWIFT/NPSE).

Initial spatial spanwise frequency spectra indicated the presence of multiple modes, whose contribution was dependent on the element shape. The initial evolution of disturbances could be obtained directly from the DNS roughness solutions or from the stability analyses. The DNS and DNS/NPSE produced nearly identical results for initial development of the disturbances. Because of the amplitude ratio involved in the definition of the $N$ factor, its initial evolution was insensitive to elemental height in describing growth of the crossflow instability. The initial growth of the velocity amplitude displayed a nonlinear dependence on elemental height, indicating the necessity for performing a DNS for each roughness configuration in order to obtain meaningful perturbation quantities that may then be used to carry out stability calculations. Nonlinear growth rates of the disturbances emphasized the importance of using the NPSE, as opposed to less sophisticated linear methods. The predicted downstream evolution of disturbances seem to correlate reasonably well with the experimentally observed features of transition.

It is believed that the stability approach described here has coupled several key methodologies for investigating receptivity and the evolution of crossflow vortices. The technique provides a framework for relating micron-sized roughness elements with the transition location on a swept wing at realistic flight Reynolds numbers. This procedure may also be useful in studying the application of subcritically spaced roughness for laminar flow control and the effects of natural surface conditions. With regard to the later, the work of Downs et al. [69] provides experimental results for a reproducible distributed rough surface.

## Acknowledgments

## References

[1] Arnal, D., "Three-Dimensional Boundary Layers: Laminar-Turbulent Transition," *Computation of Three-Dimensional Boundary Layers Including Separation*, AGARD Rept. 741, Neuilly-sur-Seine, France, Feb. 1987.

[2] Reibert, M. S., and Saric, W. S., "Review of Swept-Wing Transition," AIAA Paper 1997-1816, June–July 1997.

[3] White, E. B., Saric, W. S., Gladden, R. D., and Gabet, P. M., "Stages of Swept-Wing Transition," AIAA Paper 2001-0271, Jan. 2001.

[4] Saric, W. S., and Reed, H. L., "Crossflow Instabilities—Theory & Technology," AIAA Paper 2003-771, Jan. 2003.

[5] Saric, W. S., Reed, H. L., and White, E. B., "Stability and Transition of Three-Dimensional Boundary Layers," *Annual Review of Fluid Mechanics*, Vol. 35, Jan. 2003, pp. 413–440.
doi:10.1146/annurev.fluid.35.101101.161045

[6] Reed, H. L., and Saric, W. S., "Transition Mechanisms for Transport Aircraft," AIAA Paper 2008-3743, June 2008.

[7] Bippes, H., "Basic Experiments on Transition in Three-Dimensional Boundary Layers Dominated by Crossflow Instability," *Progress in Aerospace Sciences*, Vol. 35, No. 4, May 1999, pp. 363–412.
doi:10.1016/S0376-0421(99)00002-0

[8] Kachanov, Y. S., "Three-Dimensional Receptivity of Boundary Layers," *European Journal of Mechanics, B/Fluids*, Vol. 19, No. 5, Sep. 2000, pp. 723–744.
doi:10.1016/S0997-7546(00)90102-X

[9] Choudhari, M., and Streett, C., "Boundary Layer Receptivity Phenomena in Three-Dimensional and High-Speed Boundary Layers,"

AIAA Paper 90-5258, Oct. 1990.

[10] Deyhle, H., and Bippes, H., "Disturbance Growth in an Unstable Three-Dimensional Boundary Layer and Its Dependence on Environmental Conditions," *Journal of Fluid Mechanics*, Vol. 316, June 1996, pp. 73–113.
doi:10.1017/S0022112096000456

[11] Radeztsky, R. H., Reibert, M. S., and Saric, W. H., "Effect of Isolated Micron-Sized Roughness on Transition in Swept-Wing Flows," *AIAA Journal*, Vol. 37, No. 11, Nov. 1999, pp. 1370–1377.
doi:10.2514/2.635

[12] White, E. B., and Saric, W. S., "Secondary Instability of Crossflow Vortices," *Journal of Fluid Mechanics*, Vol. 525, Feb. 2005, pp. 275–308.
doi:10.1017/S002211200400268X

[13] Saric, W. S., Carrillo, R. B., and Reibert, M. S., "Leading-Edge Roughness as a Transition Control Mechanism," AIAA Paper 98-0781, Jan. 1998.

[14] Saric, W. S., Reed, H. L., and Banks, D. W., "Flight Testing of Laminar Flow Control in High-Speed Boundary Layers," NATO, Rept. RTO-MP-AVT-111, Brussels, 2004, pp. 32-1–32-8.

[15] Carpenter, A. L., Saric, W. S., and Reed, H. L., "In-Flight Receptivity Experiments on a 30-Degree Swept-Wing Using Micron-Sized Discrete Roughness Elements," AIAA Paper 2009-590, Jan. 2009.

[16] Carpenter, A. L., Saric, W. S., and Reed, H. L., "Roughness Receptivity in Swept-Wing Boundary Layers—Experiments," *International Journal of Engineering Systems Modelling and Simulation*, Vol. 2, No. 1/2, Mar. 2010, pp. 128–138.
doi:10.1504/IJESMS.2010.031877

[17] Crouch, J. D., "Receptivity of Three-Dimensional Boundary Layers," AIAA Paper 93-0074, Jan. 1993.

[18] Choudhari, M., "Roughness-Induced Generation of Crossflow Vortices in Three-Dimensional Boundary Layers," *Theoretical and Computational Fluid Dynamics*, Vol. 6, No. 1, Feb. 1994, pp. 1–30.
doi:10.1007/BF00417924

[19] Ng, L. L., and Crouch, J. D., "Roughness-Induced Receptivity to Crossflow Vortices on a Swept Wing," *Physics of Fluids*, Vol. 11, No. 2, Feb. 1999, pp. 432–438.
doi:10.1063/1.869860

[20] Bertolotti, F. P., "Receptivity of Three-Dimensional Boundary-Layers to Localized Roughness and Suction," *Physics of Fluids*, Vol. 12, No. 7, July 2000, pp. 1799–1809.
doi:10.1063/1.870428

[21] Collis, S. S., and Lele, S. K., "Receptivity to Surface Roughness Near a Swept Leading Edge," *Journal of Fluid Mechanics*, Vol. 380, Feb. 1999, pp. 141–168.
doi:10.1017/S0022112098003449

[22] Janke, E., "Receptivity and Transition Control of Swept-Wing Boundary-Layers; Effects of Surface Curvature and Nonlinearity," AIAA Paper 2001-2980, June 2001.

[23] Joslin, R. D., and Streett, C. L., "The Role of Stationary Cross-Flow Vortices in Boundary-Layer Transition on Swept Wings," *Physics of Fluids*, Vol. 6, No. 10, Oct. 1994, pp. 3442–3453.
doi:10.1063/1.868401

[24] Haynes, T. S., and Reed, H. L., "Simulation of Swept-Wing Vortices Using Nonlinear Parabolized Stability Equations," *Journal of Fluid Mechanics*, Vol. 405, Feb. 2000, pp. 325–349.
doi:10.1017/S0022112099007260

[25] Hogberg, M., and Henningson, D., "Secondary Instability of Crossflow Vortices in Falkner-Skan-Cooke Boundary Layers," *Journal of Fluid Mechanics*, Vol. 368, Aug. 1998, pp. 339–357.
doi:10.1017/S0022112098001931

[26] Malik, M. R., Li, F., Choudhari, M. M., and Chang, C.-L., "Secondary Instability of Crossflow Vortices and Swept-Wing Boundary-Layer Transition," *Journal of Fluid Mechanics*, Vol. 399, Nov. 1999, pp. 85–115.
doi:10.1017/S0022112099006291

[27] Koch, W., Bertolotti, F. P., Stolte, A., and Hein, S., "Nonlinear Equilibrium Solutions in a Three-Dimensional Boundary Layer and Their Secondary Instabilities," *Journal of Fluid Mechanics*, Vol. 406, Mar. 2000, pp. 131–174.
doi:10.1017/S0022112099007387

[28] Janke, E., and Balakumar, P., "On the Secondary Instability of Three-Dimensional Boundary Layers," *Theoretical and Computational Fluid Dynamics*, Vol. 14, No. 3, Sep. 2000, pp. 167–194.
doi:10.1007/s001620050135

[29] Wassermann, P., and Kloker, M., "Mechanisms and Passive Control of Crossflow-Vortex-Induced Transition in a Three-Dimensional Boundary Layer," *Journal of Fluid Mechanics*, Vol. 456, April 2002, pp. 49–84.

doi:10.1017/S0022112001007418

[30] Jiang, L., Chang, C.-L., Choudhari, M., and Liu, C., "Cross-Validation of DNS and PSE Results for Instability Wave Propagation in Compressible Boundary Layers Past Curvilinear Surfaces," AIAA Paper 2003-3555, June 2003.

[31] Jiang, L., Choudhari, M., Chang, C.-L., and Liu, C., "Direct Numerical Simulations of Crossflow Disturbances in Supersonic Boundary Layers," AIAA Paper 2004-589, Jan. 2004.

[32] Piot, E., Casalis, G., and Terracol, M., "Direct Numerical Simulation of the Crossflow Instabilities Induced by a Periodic Roughness Array on a Swept Cylinder: Receptivity and Stability Investigations," AIAA Paper 2007-3976, June 2007.

[33] Piot, E., and Casalis, G., "Receptivity of Crossflow Instabilities to a Periodic Roughness Array on a Swept Cylinder: Investigation of the Roughness Size Influence," AIAA Paper 2008-502, Jan. 2008.

[34] Steinbrenner, J. P., Chawner, J. P., and Fouts, C. L., "The GRIDGEN 3D Multiple Block Grid Generation System, Volume II: User's Manual," Wright Research and Development Center, TR WRDC-TR-90-3022, Wright-Patterson AFB, OH, Feb. 1991.

[35] Rizzetta, D. P., and Visbal, M. R., "Direct Numerical Simulation of Flow Past an Array of Distributed Roughness Elements," *AIAA Journal*, Vol. 45, No. 8, Aug. 2007, pp. 1967–1976.
doi:10.2514/1.25916

[36] Sherer, S. E., "Further Analysis of High-Order Overset Grid Method with Applications," AIAA Paper 2003-3839, June 2003.

[37] Sherer, S. E., and Scott, J. N., "High-Order Compact Finite Difference Methods on General Overset Grids," *Journal of Computational Physics*, Vol. 210, No. 2, Dec. 2005, pp. 459–496.
doi:10.1016/j.jcp.2005.04.017

[38] Beam, R., and Warming, R., "An Implicit Factored Scheme for the Compressible Navier–Stokes Equations," *AIAA Journal*, Vol. 16, No. 4, April 1978, pp. 393–402.
doi:10.2514/3.60901

[39] Gordnier, R. E., and Visbal, M. R., "Numerical Simulation of Delta-Wing Roll," AIAA Paper 93-0554, Jan. 1993.

[40] Jameson, A., Schmidt, W., and Turkel, E., "Numerical Solutions of the Euler Equations by Finite Volume Methods Using Runge-Kutta Time Stepping Schemes," AIAA Paper 81-1259, June 1981.

[41] Pulliam, T. H., and Chaussee, D. S., "A Diagonal Form of an Implicit Approximate-Factorization Algorithm," *Journal of Computational Physics*, Vol. 39, No. 2, Feb. 1981, pp. 347–363.
doi:10.1016/0021-9991(81)90156-X

[42] Lele, S. A., "Compact Finite Difference Schemes with Spectral-Like Resolution," *Journal of Computational Physics*, Vol. 103, No. 1, Nov. 1992, pp. 16–42.
doi:10.1016/0021-9991(92)90324-R

[43] Visbal, M. R., and Gaitonde, D. V., "High-Order-Accurate Methods for Complex Unsteady Subsonic Flows," *AIAA Journal*, Vol. 37, No. 10, Oct. 1999, pp. 1231–1239.
doi:10.2514/2.591

[44] Gaitonde, D., Shang, J. S., and Young, J. L., "Practical Aspects of High-Order Accurate Finite Volume Schemes for Electromagnetics," AIAA Paper 97-0363, Jan. 1997.

[45] Gaitonde, D., and Visbal, M. R., "High-Order Schemes for Navier–Stokes Equations: Algorithm and Implementation into FDL3DI," Air Force Research Laboratory, TR AFRL-VA-WP-TR-1998-3060, Wright-Patterson AFB, OH, Aug. 1998.

[46] Gordnier, R. E., "Computation of Delta-Wing Roll Maneuvers," *Journal of Aircraft*, Vol. 32, No. 3, May 1995, pp. 486–492.
doi:10.2514/3.46746

[47] Visbal, M. R., "Computational Study of Vortex Breakdown on a Pitching Delta Wing," AIAA Paper 93-2974, July 1993.

[48] Visbal, M., Gaitonde, D., and Gogineni, S., "Direct Numerical Simulation of a Forced Transitional Plane Wall Jet," AIAA Paper 98-2643, June 1998.

[49] Rizzetta, D. P., Visbal, M. R., and Stanek, M. J., "Numerical Investigation of Synthetic-Jet Flowfields," *AIAA Journal*, Vol. 37, No. 8, Aug. 1999, pp. 919–927.
doi:10.2514/2.811

[50] Rizzetta, D. P., and Visbal, M. R., "Direct Numerical Simulation of Flow Past an Array of Distributed Roughness Elements," AIAA Paper 2006-3527, June 2006.

[51] Gaitonde, D. V., Visbal, M. R., and Roy, S., "Control of Flow Past a Wing Section with Plasma-Based Body Forces," AIAA Paper 2005-5302, June 2005.

[52] Visbal, M. R., and Gaitonde, D. V., "Control of Vortical Flows Using Simulated Plasma Actuators," AIAA Paper 2006-0505, Jan. 2005.

[53] Visbal, M. R., Gaitonde, D. V., and Roy, S., "Control of Transitional and Turbulent Flows Using Plasma-Based Actuators," AIAA Paper 2006-3230, June 2006.

[54] Rizzetta, D. P., and Visbal, M. R., "Numerical Investigation of Plasma-Based Flow Control for Transitional Highly Loaded Low-Pressure Turbine," *AIAA Journal*, Vol. 45, No. 10, Oct. 2007, pp. 2554–2564.
doi:10.2514/1.29602

[55] Rizzetta, D. P., and Visbal, M. R., "Plasma-Based Flow Control Strategies for Transitional Highly Loaded Low-Pressure Turbines," *Journal of Fluids Engineering*, Vol. 130, No. 4, April 2008, Paper 041104.
doi:10.1115/1.2903816

[56] Rizzetta, D. P., and Visbal, M. R., "Large Eddy Simulation of Plasma-Based Control Strategies for Bluff Body Flow," *AIAA Journal*, Vol. 47, No. 3, Mar. 2009, pp. 717–729.
doi:10.2514/1.39168

[57] Rizzetta, D. P., and Visbal, M. R., "Numerical Investigation of Transitional Flow Through a Low-Pressure Turbine Cascade," AIAA Paper 2003-3587, June 2003.

[58] Rizzetta, D. P., Visbal, M. R., and Blaisdell, G. A., "A Time-Implicit High-Order Compact Differencing and Filtering Scheme for Large-Eddy Simulation," *International Journal for Numerical Methods in Fluids*, Vol. 42, No. 6, June 2003, pp. 665–693.
doi:10.1002/fld.551

[59] Rizzetta, D. P., and Visbal, M. R., "Application of Large-Eddy Simulation to Supersonic Compression Ramps," *AIAA Journal*, Vol. 40, No. 8, Aug. 2002, pp. 1574–1581.
doi:10.2514/2.1826

[60] Rizzetta, D. P., and Visbal, M. R., "Large-Eddy Simulation of Supersonic Cavity Flowfields Including Flow Control," *AIAA Journal*, Vol. 41, No. 8, Aug. 2003, pp. 1452–1462.
doi:10.2514/2.2128

[61] "Advances in Laminar-Turbulent Transition Modelling," VKI Lecture Series, von Karman Inst. for Fluid Dynamics, Rhode St. Genese, Belgium, 2009.

[62] Herbert, T., "Parabolized Stability Equations," *Annual Review of Fluid Mechanics*, Vol. 29, Jan. 1997, pp. 245–283.
doi:10.1146/annurev.fluid.29.1.245

[63] Saric, W. S., "Görtler Vortices," *Annual Review of Fluid Mechanics*, Vol. 26, Jan. 1994, pp. 379–409.
doi:10.1146/annurev.f1.26.010194.002115

[64] Haynes, T. S., "Nonlinear Stability and Saturation of Crossflow Vortices in Swept-Wing Boundary Layers," Ph.D. Thesis, Arizona State Univ., Tempe, AZ, 1996.

[65] Bertolotti, F. P., and Joslin, R. D., "Effect of Far-Field Boundary Conditions on Boundary-Layer Transition," *Journal of Computational Physics*, Vol. 118, No. 2, May 1995, pp. 392–395.
doi:10.1006/jcph.1995.1109

[66] Rhodes, R. G., Carpenter, A. L., Reed, H. L., and Saric, W. L., "CFD Analysis of Flight-Test Configuration for LFC on Swept Wings," AIAA Paper 2008-7336, Aug. 2008.

[67] Rhodes, R. G., Reed, H. L., Saric, W. S., Carpenter, A. L., and Neale, T. P., "Roughness Receptivity in Swept-Wing Boundary Layers—Computations," *International Journal of Engineering Systems Modelling and Simulation*, Vol. 2, Nos. 1–2, Mar. 2010, pp. 139–148.
doi:10.1504/IJESMS.2010.031878

[68] Reibert, M. S., Saric, W. S., Carrillo, R. B., and Chapman, K. L., "Experiments in Nonlinear Saturation of Stationary Crossflow Vortices in a Swept-Wing Boundary Layer," AIAA Paper 1996-0184, Jan. 1996.

[69] Downs, R. S., White, E. B., and Denissen, N. A., "Transient Growth and Transition Induced by Random Distributed Roughness," *AIAA Journal*, Vol. 46, No. 2, Feb. 2008, pp. 451–462.
doi:10.2514/1.31696

T. Jackson
*Associate Editor*